Local Ferromagnetic Resonance Measurements of Mesoscopically Patterned Ferromagnets Using Deterministically Placed Nanodiamonds

Jeffrey Rable, Benjamin Piazza,[†] Jyotirmay Dwivedi, and Nitin Samarth[*]
Department of Physics, Pennsylvania State University, University Park, Pennsylvania 16802, USA

(Received 30 January 2022; revised 28 June 2022; accepted 28 October 2022; published 1 December 2022)

Nitrogen-vacancy centers in diamond have recently been established as effective sensors of the magnetization dynamics in vicinal ferromagnetic materials. We demonstrate sub-100-nm placement accuracy of nitrogen-vacancy-containing nanodiamonds and use these as local sensors that probe optically detected ferromagnetic resonance in mesoscopically patterned Permalloy islands. These measurements reveal variations in the ferromagnetic resonance signal at different sites on these structures with distinct behavior in the edge and the bulk of patterned features. These test measurements establish an easily implemented approach for spatially targeted measurements of spin dynamics in mesoscale ferromagnets. In principle, the methodology can also be extended to local studies of nanoscale ferromagnets, such as single magnetic nanowires and nanoparticles.

DOI: 10.1103/PhysRevApplied.18.064004

I. INTRODUCTION

Contemporary problems of interest in spintronics often require knowledge of the dynamical behavior of magnonic (spin-wave) excitations in patterned ferromagnetic devices. For example, this information is useful in the creation and characterization of magnon quantum buses [1,2] and other magnonic devices such as spin-based transistors [3]. The nitrogen-vacancy (N-V) center in diamond has emerged as an effective nonperturbative local probe for characterizing the magnetic properties of such systems [4]. N-V center-based local magnetometry has provided insights into static spin configurations of skyrmions [5,6] and magnetic domain walls [7], as well as the dynamical behavior of magnons [8–11] and vortices [12]. In the latter context, it is worthwhile to develop techniques that allow local measurements of ferromagnetic resonance (FMR) at targeted locations in a ferromagnetic sample or device.

Continuous wave N-V center-based optically detected ferromagnetic resonance (ODFMR) measurements rely on the quenching of the N-V center fluorescence when a vicinal ferromagnet meets the conditions for FMR [8]. This is attributed to an increased magnon density and an accompanying enhancement of the magnetic field noise sensed by the N-V centers, thus leading to increased spin relaxation [9]. Local measurements of ODFMR have relied on stochastic distribution of dropcast nanodiamonds [8, 13], stochastic distribution of N-Vs in a diamond film [12–15], proximate placement of a diamond nanobeam [9,11], and chemically patterned directed assembly of nanodiamonds [10]. In principle, scanned probe N-V center magnetometry could provide a means of carrying out local ODFMR with imaging capability. However, since N-V detection of ODFMR rapidly decreases in sensitivity with increasing sample-probe distance [15], N-V scanning probe measurements of ODFMR may be constrained by the tip-sample distances that are typically greater than about 100 nm [7,16,17]. Although one scanning N-V technique allows for smaller tip-sample separation (approximately 30 nm) [5], it would be technically challenging to engineer effective excitation of the FMR in a ferromagnetic sample in this geometry; to date, the only published scanning probe measurements report distances on the order of hundreds of nm [18]. Furthermore, our direct placement technique is more broadly accessible than scanning probe setups; commercial setups are expensive while bespoke setups require complex instrumentation, and both require specialized diamond tip fabrication. As an aside, we note that local magnetization dynamics of ferromagnets can also be effectively probed and imaged via a completely different method, namely scanning ferromagnetic resonance force microscopy (FMRFM), which uses a microscale force cantilever to detect FMR with approximately 100–200 nm spatial resolution [19–22]. As with N-V-center-based ODFMR, the FMRFM technique is amenable to measurements at ambient temperature. However, in contrast with N-V-center ODMFR, the FMRFM method requires more sophisticated instrumentation and relies on magnetic probes, which can perturb the sample dynamics and limit resolution [23]. Thus, a question of interest is whether one can develop a simpler approach for locally measuring FMR at targeted sites on a

[*]nsamarth@psu.edu
[†]Current address: Network Science Institute, Northeastern University, Boston, MA 02115, USA.

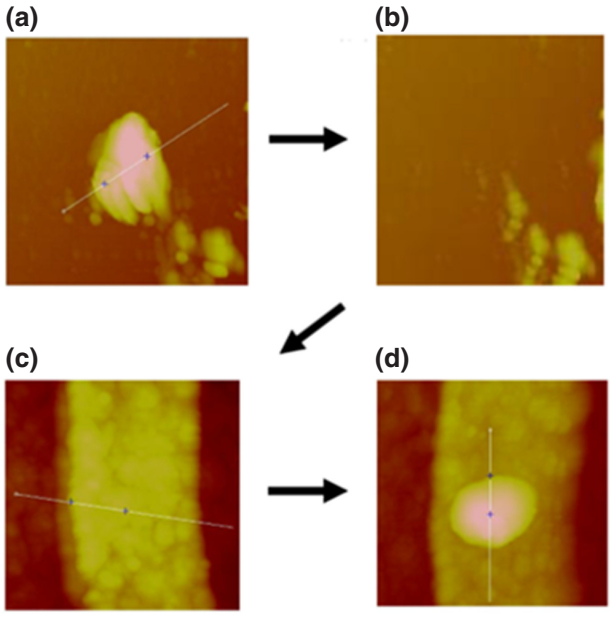

FIG. 1. Demonstration of the nanodiamond placement process with a 40-nm-diameter nanodiamond (a). After lifting the nanodiamond and confirming it is no longer on the sample (b), we move over to the deposition site, a 100-nm-wide Permalloy nanowire (c). Then, we can deposit via ramp or lift mode and confirm placement via another scan (d).

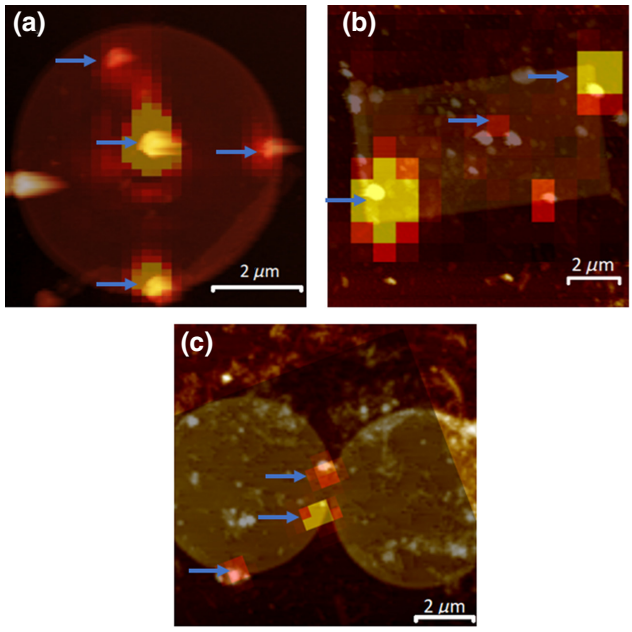

FIG. 2. AFM images of the measured Permalloy features with superimposed scanning confocal fluorescence images showing where N-V-containing nanodiamonds are located. Additional blue arrows are added to mark the nanodiamonds that are measured on. (a) A 6-μm-diameter, 10-nm-thick Permalloy circle with nanodiamonds located near the top edge, bottom edge, right edge, and center. The large feature on the left edge of the circle is a dust particle or piece of leftover photoresist that is on the sample prior to placement and does not fluoresce. (b) A 6-μm-wide, 12-μm-long rectangular feature with three nanodiamonds around the edges and a single nanodiamond in the bulk. (c) Two 6-μm-diameter, 10-nm-thick Permalloy circles connected at the edges. Nanodiamonds are located at the periphery of the left disk and near the junction between the disks.

mesoscopic or nanoscale ferromagnetic structure without having to resort to the sophisticated instrumentation required by scanning microscopy techniques.

In this paper, we demonstrate the use of an atomic force microscope (AFM) to achieve well-controlled positioning of N-V-containing nanodiamonds as FMR sensors, with sizes between 40–100 nm and with sub-100-nm accuracy. We use these deterministically placed nanodiamonds to perform local ODFMR measurements of mesoscale (5–10 μm lateral size) features patterned in ferromagnetic Permalloy thin films. Although similar to a "pick-and-place" technique previously reported for assembling nanodiamonds at desired locations [24,25], this approach has not yet been exploited to probe the localized magnetization dynamics of magnetic materials. We note that chemically patterned directed assembly of nanodiamonds has been effectively used for probing ODFMR in YIG devices [10]; however, the measured locations are constrained in advance by lithographic patterning and subject to overlay error. We seek a more flexible approach that allows the measured locations to be varied at will. The placement precision in our proof-of-concept demonstration can, in principle, also allow for the targeted measurement of smaller nanoscale structures, such as nanowires, or of localized modes in larger structures, such as edge modes and defect modes.

II. METHODS

A. Nanodiamond placement and ODFMR

We first describe the experimental approach for deterministic placement. We begin with a sample containing patterned Permalloy structures in the center and drop cast an aqueous suspension containing 100-nm-diameter nanodiamonds with 3 ppm N-V centers onto the edge of the sample. This is done to avoid directly depositing nanodiamonds onto the features. The suspension concentration used is 0.01 mg/ml, and it is sonicated for 1 h prior to placement in order to separate glomerates of nanodiamonds. By using 100-nm nanodiamonds for the measurements in this work, our resulting N-V-sample separation averages 50 nm. However, this technique can also be used with 40-nm nanodiamonds, leading to an average separation of 20 nm. We do not attempt to place smaller particles.

Once the sample dries, we scan the area where the nanodiamonds are drop cast using a Veeco Nanoscope IIIA

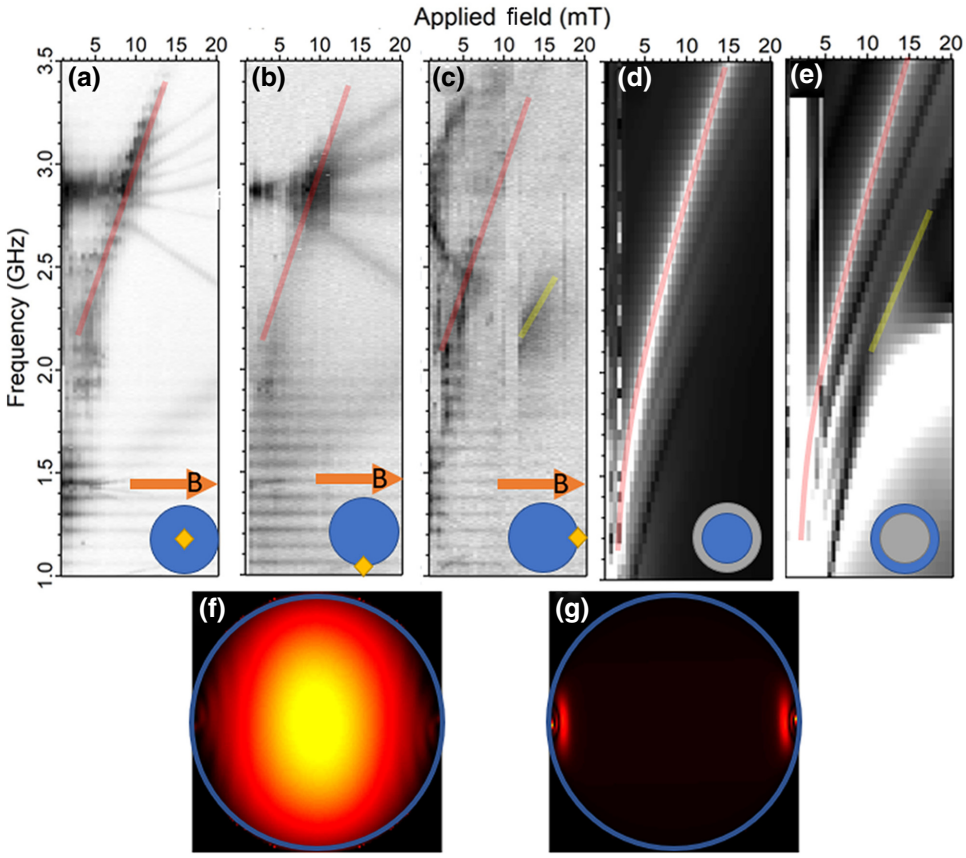

FIG. 3. ODFMR measurements using a nanodiamond located at distinct sites on a disk feature. The yellow diamonds mark the nanodiamond location. The panels show measurements performed on a nanodiamond at (a) the center of the disk, (b) the bottom of the disk, and (c) along the right edge of the disk. In each case, the primary resonance is marked with a red guide to the eye. In (c), we also mark an additional signal in yellow. (d) Micromagnetic simulations of FMR in the bulk of the disk; the entire disk is simulated, but the magnetization of the outermost 200-nm-wide annulus (gray) is excluded from the analysis. (e) Micromagnetic simulations of FMR in the edge of the disk where the whole feature is simulated but only the average magnetization of the outermost 200 nm is sampled and analyzed. (f) Simulated spatial distribution of the red mode in (d) marked with a red guide to the eye at 15 mT and 3.55 GHz. (g) Simulated spatial distribution of the edge mode marked in (e) with a yellow guide to the eye at 15 mT and 2.2 GHz.

Multimode AFM in tapping mode with a gold-coated silicon tip, which increases the probability of pickup over a standard silicon tip, likely because of stronger van der Waals forces or malleability of the gold. When we find a particle that matches the dimensions of the dispersed nanodiamonds, we zoom in on the particle [Fig. 1(a)] and enter ramp mode. Ramp mode lowers the tip into the sample at a set rate until a threshold voltage is reached, at which point, the tip is retracted. We start the ramp 1 μm away from the sample, ramp at a velocity of approximately 500 nm/s, and have the tip retract at a threshold voltage between 1.8 and 2.5 V. Then, we ramp into the nanodiamond and rescan the area where it was in the prior scan to confirm pickup [Fig. 1(b)]. If the nanodiamond remains at the site, we ramp in again until it is picked up or attempt pickup on a different particle.

If the nanodiamond does not appear on the postramp scan, indicating that it was picked up, we can begin the placement process by moving the AFM tip to our patterned features. With the nanodiamond still attached to the tip, we can scan the sample looking for the feature that we want to deposit the particle on [Fig. 1(c)]. When we find the device, we either repeat the process used in pickup, ramping into the feature until the nanodiamond dislodges, or we scan across the sample at a constant height below the surface using the AFM's lift mode, scraping the nanodiamond-coated tip along until it dislodges. While this second method works more consistently, it risks scratching the sample if the tip is dug into the feature. Finally, with the diamond dislodged, we perform a final scan to confirm that the nanodiamond is in the desired location [Fig. 1(d)]. We caution that we do not yet have a systematic measure of the success rate of the pickup method. The repeatability of the technique appears to depend on factors that are not completely understood yet and varies with the details of the drop casting and the substrate;

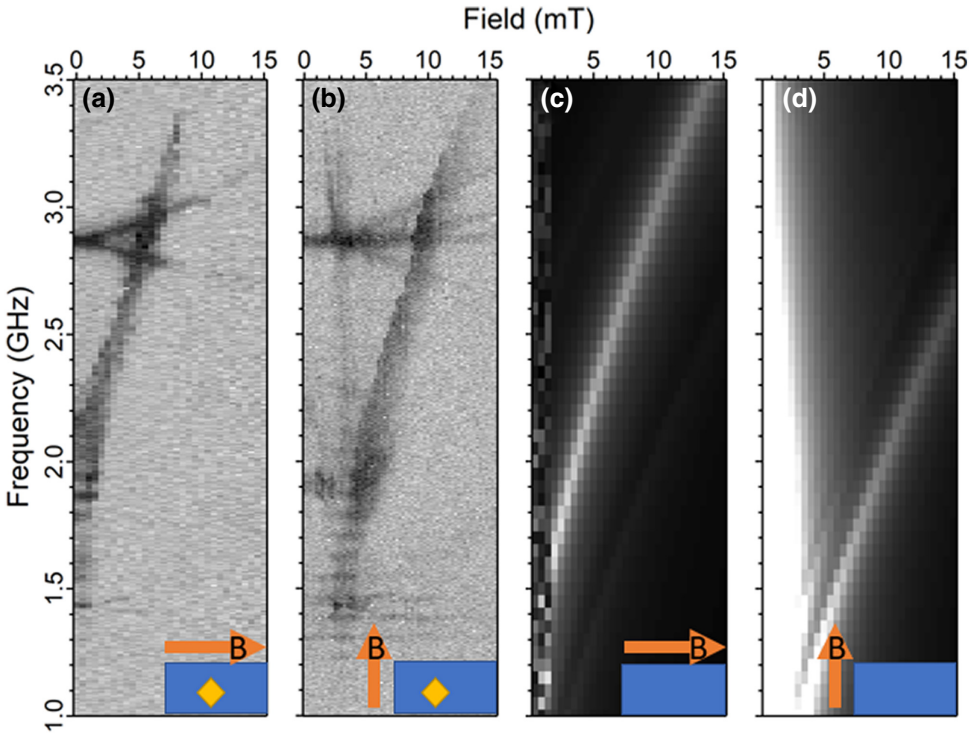

FIG. 4. Measurement of ODFMR using a nanodiamond in the bulk of a rectangular Permalloy island with the applied magnetic field oriented along (a) the longitudinal easy axis and (b) along the transverse hard axis. The difference in N-V center ground-state splittings around 2.87 GHz is the result of the different fields along the N-V axis and, at low fields in (b), possibly the result of stray fields from the unsaturated bottom edge of the island. The corresponding micromagnetic simulations of the FMR with the applied magnetic field oriented along (c) the longitudinal easy axis and (d) the transverse hard axis. These results match qualitatively, but our results are at a higher frequency.

sometimes we have a 0% success rate, but drop casting new nanodiamonds on will increase the pickup probability, approaching 100% success. However, once a nanodiamond is picked up, placement success is approximately 90%. We believe that the failure rate is the result of a nanodiamond falling off the tip prematurely when manually moving the tip across the sample, rather than getting stuck on the tip, because subsequent placement with the same tip does not result in double placement.

Once a particle is placed, it is confirmed to be an N-V-containing nanodiamond via fluorescence imaging and detection of the N-V ground-state transition at 2.87 GHz. However, because of the tight size distribution and high density of our commercial nanodiamonds in the drop cast area, placement of non-nanodiamond particles occurs very rarely. One major downside of this placement technique is that we have no control over the orientation of the nanodiamond, leading to random N-V orientation. Additionally, determining the orientation of the nanodiamond after placement can be complicated by stray fields from proximal ferromagnetic features.

For optical polarization and readout of the N-V center fluorescence, we use a 532-nm continuous-wave laser providing 1 mW of power at the back of our objective lens and an ID Quantique ID100 avalanche photodiode. A scanning mirror scans across the surface for imaging and allows focusing on a site for ODFMR measurements. A static magnetic field is applied using a permanent N52 magnet mounted on a highly repeatable stepper motor linear stage. The applied field is calibrated in the plane of the sample using a single-crystal diamond film containing N-V centers; this is achieved using the known orientations and the Zeeman splitting of the N-V electronic ground-state spin transition. During the ODFMR measurements, a microwave magnetic field is applied via a 25-μm-diameter gold wire run across the sample. This microwave field both drives FMR in the magnetic features and the N-V spin state transitions. Additionally, when FMR is driven in the sample, new, higher frequency magnons are generated via scattering and thermal mechanisms. The dipolar field noise generated by these incoherent magnons also affects the N-V spin state transitions; this effect is believed to be responsible for the detection of FMR via an optical contrast even though the FMR is driven at frequencies off resonant from those that drive the N-V spin transitions [9].

B. Micromagnetic simulations

Prior to our measurements, we perform micromagnetic simulations of the FMR modes in patterned Permalloy

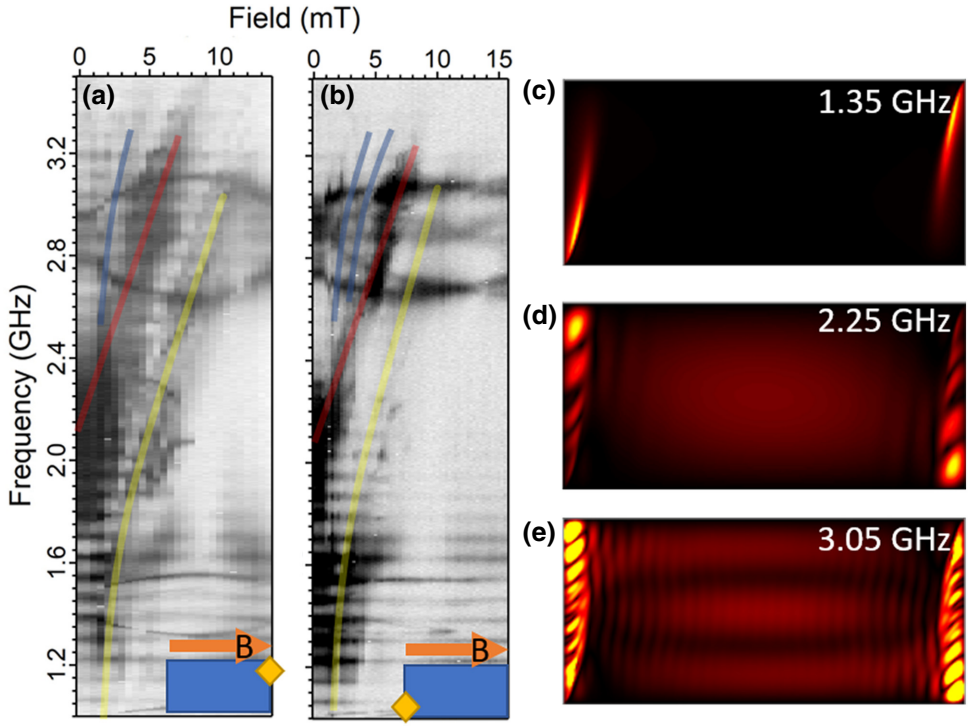

FIG. 5. Measurement of ODFMR using nanodiamonds along the edges of a rectangular Permalloy island with an applied magnetic field oriented along the longitudinal easy axis. (a) Measurement of the upper right corner of the rectangle performed at a higher microwave power; we see the bulk mode (red guide to the eye) from Fig. 4(a), which has a simulated spatial profile shown in (d), a lower-frequency edge mode (yellow guide to the eye) simulated in (c), and a higher-frequency bulk mode (blue guide to the eye) with simulated in (e). (b) Lower microwave power measurement on the left edge near the bottom of the rectangle, which shows the same features as (a), but with less broadening. This more clearly shows the higher-frequency modes, the lowest two of which are marked with blue guides to the eye. (c)–(e) Simulated spatial profiles of the yellow edge mode at 1.35 GHz, red bulk mode at 2.25 GHz, and higher-order blue bulk mode at 3.05 GHz, respectively, at 5 mT. These simulations are done with a small misalignment angle to break the symmetry of the system and replicate the true direction of our applied magnetic field.

features identical to those measured experimentally. The Permalloy film thickness in all these simulations is 10 nm. The simulations are performed with the Mumax3 software package, which uses the Landau-Lifshitz-Gilbert equation:

$$\frac{\partial \vec{m}}{\partial t} = \gamma_{\mathrm{LL}} \frac{1}{1+\alpha^2} (\vec{m} \times \vec{B_{\mathrm{eff}}} + \alpha(\vec{m} \times (\vec{m} \times \vec{B_{\mathrm{eff}}}))) \quad (1)$$

to calculate the evolution of the reduced magnetization $\vec{m}$ of finite ferromagnetic cells. In Eq. (1), α is the Gilbert damping of the material, γ_{LL} is the gyromagnetic ratio of the material, and B_{eff} is the effective magnetic field at that cell, which includes contributions from external, demagnetization, exchange, and anisotropy fields [26].

The simulations are performed using $5 \times 5 \times 10$ nm cells and the geometries consist of Permalloy features with a saturation magnetization M_s of 8×10^5 A/m, exchange constant A_{ex} of 1.3×10^{-11} J/m, and Gilbert damping α of 0.0063.

After defining the sample geometry, the system is given an initial magnetization pointing along the (0, 0, 1) direction out of the plane of the film and allowed to relax to the minimum energy state in the applied bias field, which ranged from 1 to 30 mT in our simulations.

To excite the system, we apply a Gaussian pulse with a 20-ps full width half maximum and a 0.5-mT amplitude. The system is then allowed to freely evolve in time for 20 ns and average magnetization is sampled every 5 ps. Finally, we use a discrete fast Fourier transform (DFFT) to analyze the data in the frequency domain. Using the above sampling rates and simulation lengths, we obtain a resolution of 50 MHz.

For spatially resolved imaging of modes, we sample the magnetization in $50 \times 50 \times 10$ nm segments of the sample and display the results as the relative intensity of the DFFT of each segment at the resonance frequency.

III. RESULTS

We begin with measurements on a 6-μm-diameter, 10-nm-thick circular Permalloy disk [Fig. 2(a)] with the intent of searching for edge modes along the side of the disc perpendicular to the applied magnetic field. We measure three nanodiamonds placed on the disc, one in the

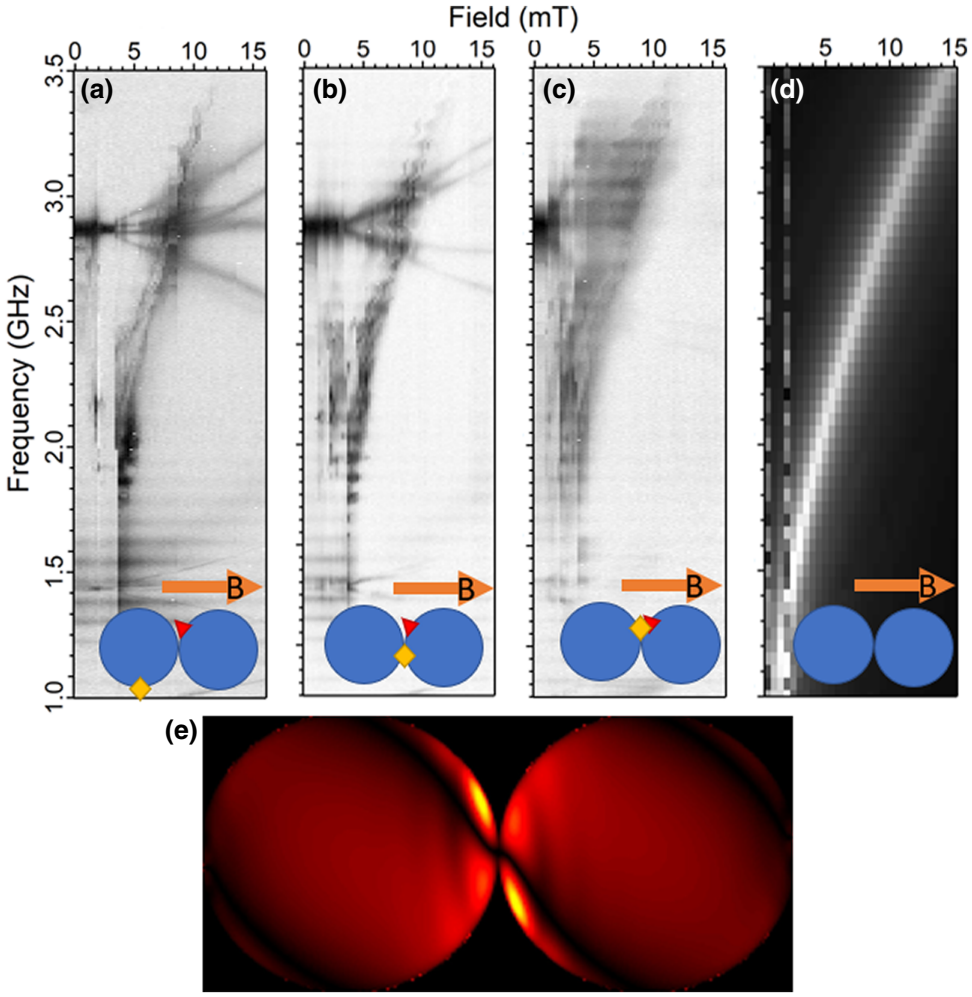

FIG. 6. ODFMR measurements using a nanodiamond located at different sites along the edge of a circular double disk feature where the disks meet to form a constriction. The yellow diamonds mark the nanodiamond location and the red triangle represents the defect site. Measurements are made at three distinct sites: (a) far away from the constriction; (b) near the constriction; (c) on the opposite end of the constriction, close to a misfabricated edge. (d) Micromagnetic simulations of FMR in the double circle feature. (e) Micromagnetic simulations of the resonance in (d) at 15 mT. There is a small misalignment angle added to break the symmetry of the system and replicate our experimental measurement more closely.

center, one on the bottom edge, and one on the right edge. We find that measurements in the center of the feature [Fig. 3(a)] match the results of our simulations [Fig. 3(d)] well, with a small shift from our measured results. We also find that the results along the bottom of the circle, which lies parallel to the applied field, match these results, albeit with much weaker coupling. In measurements along the right edge [Fig. 3(c)], perpendicular to the applied field, we detect both the primary mode (marked in red) from Figs. 3(a) and 3(b), which becomes substantially dimmer past 6.5 mT, as well as an additional edge mode (marked in yellow) that appears at 12 mT [Fig. 3(g)]. We believe that we detect only this edge mode and not the lower frequency ones shown in our simulations [Fig. 3(e)] because of a magnetic field misalignment, which will confine the lower-order edge modes to a small section of the sample away from our nanodiamond. We also note that the N-V ground-state transition exhibits a wider splitting at this site because of the on-axis stray fields from the disc.

Next, we perform similar measurements on a 12 $\times$ 6 μm^2 Permalloy rectangle [Fig. 2(b)] to demonstrate further detection of edge modes. We first perform a control measurement in the bulk of the rectangle (Fig. 4), confirming that we detect the expected easy- and hard-axis FMR modes under different applied field orientation.

We then perform measurements at two nanodiamonds placed along the edges of the feature to search for edge modes. In both measurements [Figs. 5(a) and 5(b)], we see the bulk mode detected in Fig. 4(a) and marked with a red guide, as well as a lower-frequency mode marked in yellow. The simulated spatial profile of this yellow mode is shown in Fig. 5(c), confirming that it is an edge mode

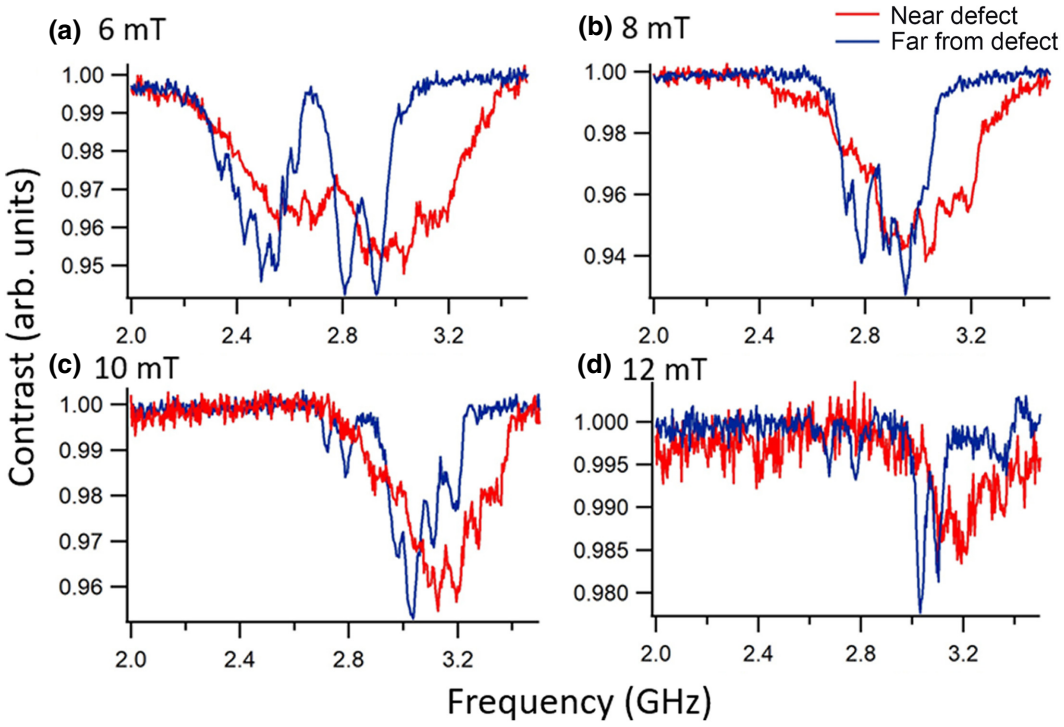

FIG. 7. Line cuts of the double disk data taken from the two nanodiamonds near the constriction, which show substantial broadening at the site closest to the defect.

confined to the sides of the rectangle perpendicular to the applied magnetic field. Following the method reported by McMichael and Maranville [27], we can fit the Kittel equation to the edge mode to find an edge saturation field of 0.4 mT, which is likely the result of magnetic field misalignment. Additionally, we see higher-order bulk modes in Figs. 5(a) and 5(b) marked with blue guides, the lowest frequency of which is shown in Fig. 5(e). In these measurements, the N-V ground-state transition splitting is the result of stray fields from the edges of the feature.

We now discuss measurements on a feature composed of two connected 6-μm-diameter, 10-nm-thick circular Permalloy disks [Fig. 2(c)]. These features had a slight fabrication error in one of the circles near the constriction where they meet, leading to a sharp edge slightly protruding, which could cause a local distortion of the ferromagnetic resonance. We position and measure nanodiamonds at three different sites—one on the edge approximately 4 μm from the constriction, one on the pristine side of the constriction approximately 2 μm from the fabrication error, and one in the same position on the misfabricated side of the constriction, approximately 750 nm away from the error. Far away from the constriction, the data shows streaking at approximately 2 mT, and a signal that begins suddenly at approximately 4 mT [Fig. 6(a)]. Near the constriction [Fig. 6(b)], we see additional broadband noise at lower fields (between 2–4 mT), but the signal largely matches that in Fig. 6(a). On the opposite end of the constriction [Fig. 6(c)], close to the misfabricated edge, the primary resonance detected at higher fields matches the measurements at the other two sites, but an additional high-frequency resonance emerges, leaving our detection range between 5 and 10 mT. At this site, the signal up to 5 mT appears to be broadband noise, with greater contrast as the field increases. The line width also increases dramatically, as can be seen in Fig. 7; for example, it increases from 156 MHz at 10 mT at the opposite, pristine side of the constriction to 278 MHz at 10 mT. Micromagnetic simulations of FMR in the double circle feature [Fig. 6(d)] match our experimental results well for fields stronger than 4 mT. Additionally, our simulations show that one would not expect such a significant difference in power broadening between the two constriction measurement sites in a pristine double circle system, further supporting our hypothesis that the defect is responsible for the observed broadening effect [Fig. 6(e)]. We speculate that the disagreement between measurements and simulations at lower fields is caused by differences in the magnetic texture of the material, as the applied field will not saturate the ferromagnet and our simulation setup procedure does not perfectly replicate the history of the features.

IV. SUMMARY

We demonstrate a straightforward method to deterministically place N-V-containing nanodiamonds at desired

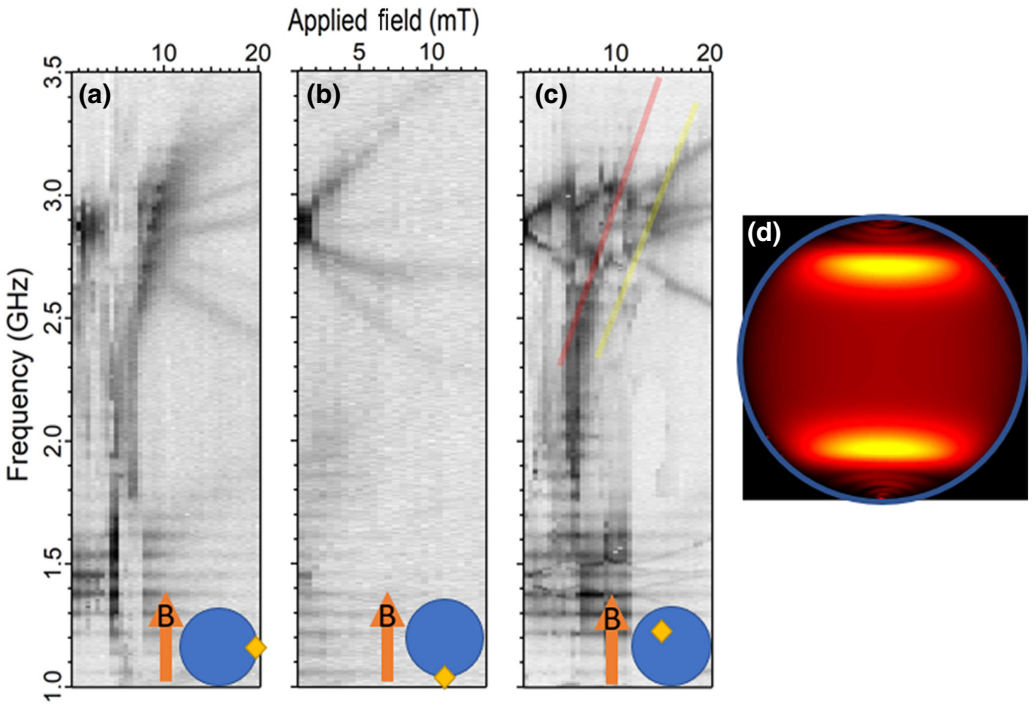

FIG. 8. ODFMR measurements on the same feature in Fig. 3 with the magnetic field rotated 90°. (a) Measurements on the right edge nanodiamond, showing a more prominent bulk-mode signal and no edge-mode signal, as expected from the simulations in Figs. 3(f) and 3(g). (b) Measurements on the bottom edge nanodiamond, showing that the previously detected faint bulk-mode signal largely vanishes. We believe that we do not see any edge modes because of the poor coupling at this site. (c) Measurements on the nanodiamond 750 nm away from the top edge of the sample. This nanodiamond detects both the bulk mode, marked with a red guide to the eye, and an additional mode at a slightly lower frequency, marked with a yellow guide to the eye. (d) Simulations showing the spatial distribution of the mode detected in (c) and marked with a yellow guide. This simulation is performed at 15 mT and 3.1 GHz.

locations on lithographically patterned ferromagnetic thin films. Using this placement, we perform local ODFMR measurements on single mesoscopic Py islands, revealing position-dependent variations in spin dynamical behavior that cannot be detected using conventional FMR measurements of ensembles of patterned islands. After demonstrating that this technique could be used to detect edge modes in a single-circle feature, we confirm this measurement via edge-mode detection in a rectangular feature. We then apply it to a more complex feature composed of two circles with a subtle fabrication error near the point of closest approach. In the vicinity of this fabrication error, we measure both a larger line width and an additional signal that did not appear in the control measurement away from the error or in our micromagnetic simulations of pristine patterns. This finding shows that local ODMFR measurements using targeted placement of nanodiamonds can provide information about the influence of defects on the spin dynamical behavior of patterned ferromagnets.

Moving forward, we see this technique being used as a more general method of measuring localized magnetization dynamics in various patterned ferromagnetic structures. For example, the technique could provide further insight into the properties of spin-wave edge modes previously detected using scanning FMRFM [21]; for example, it can be used to demonstrate splitting of uniform modes into bulk and edge localized states. It could also be used for probing the local magnetization dynamics of artificial spin ice arrays [28,29], or for the design of N-V-ferromagnet hybrid devices. Finally, because we achieve sub-100-nm placement accuracy, we believe this technique could be used to more readily explore the dynamics of single trapped domain walls, skyrmions, or other nanoscale magnetic textures in samples where relying on either stochastic assembly or template-enabled assembly may not be feasible.

ACKNOWLEDGMENTS

The authors thank Eric Kamp for initiating the N-V center project in our research group and David Awschalom for useful discussions. We are grateful to Michael Labella for his sample fabrication advice. This work was carried out by BP in part as an undergraduate honors thesis within the Schreyer Honors College at Penn State. We acknowledge support from the University of Chicago and the U.S. Department of Energy Office of Science National Quantum Information Science Research Centers (Q-NEXT).

APPENDIX

Additional measurements are also performed on the single disc feature after rotating the applied magnetic field 90°. During the sample wiring process, the center nanodiamond is dislodged, and measurements are performed on the remaining three nanodiamonds, namely, the one of the right edge of the sample, the one on the bottom edge of the sample, and the misplaced one approximately 1 μm from the top edge, which is not previously measured. We find that the nanodiamond in Fig. 8(b) no longer detects the bulk mode observed in Fig. 3(b), which could be expected from its weak coupling and the spatial distribution of the mode shown in Fig. 3(f). We believe this weak coupling is why we also do not detect an edge mode. We also find that the nanodiamond in Fig. 3(c) now detects the bulk mode more prominently and no longer detects an edge mode in Fig. 8(a), as the simulations in Figs. 3(f) and 3(g) would suggest. Finally, in Fig. 8(c), we measure the nanodiamond that is placed approximately 1 μm from the top edge, which shows the bulk mode as well as an additional, slightly lower-frequency mode. Simulations performed in Fig. 8(d) show that this mode is confined to an area approximately 1 μm wide and 1 μm from the edges of the sample, which matches well the location of the nanodiamond. Furthermore, the stray fields detected in Fig. 8(c) likely reflect the movement of a vortex; this matches results in prior studies of disks [12] and our simulations show that vortices can nucleate near the nanodiamond position.

[1] D. R. Candido, G. D. Fuchs, E. Johnston-Halperin, and M. E. Flatté, Predicted strong coupling of solid-state spins via a single magnon mode, Mater. Quantum Technol. **1**, 011001 (2020).

[2] M. Fukami, D. R. Candido, D. D. Awschalom, and M. E. Flatté, Opportunities for Long-Range Magnon-Mediated Entanglement of Spin Qubits via On- and Off-Resonant Coupling, PRX Quantum **2**, 040314 (2021).

[3] A. V. Chumak, A. A. Serga, and B. Hillebrands, Magnon transistor for all-magnon data processing, Nat. Commun. **5**, 4700 (2014).

[4] F. Casola, T. van der Sar, and A. Yacoby, Probing condensed matter physics with magnetometry based on nitrogen-vacancy centres in diamond, Nat. Rev. Mater. **3**, 17088 (2018).

[5] Y. Dovzhenko, F. Casola, S. Schlotter, T. X. Zhou, F. Büttner, R. L. Walsworth, G. S. Beach, and A. Yacoby, Magnetostatic twists in room-temperature skyrmions explored by nitrogen-vacancy center spin texture reconstruction, Nat. Commun. **9**, 2712 (2018).

[6] A. Jenkins, M. Pelliccione, G. Yu, X. Ma, X. Li, K. L. Wang, and A. C. B. Jayich, Single-spin sensing of domain-wall structure and dynamics in a thin-film skyrmion host, Phys. Rev. Mater. **3**, 083801 (2019).

[7] J.-P. Tetienne, T. Hingant, L. Martínez, S. Rohart, A. Thiaville, L. H. Diez, K. Garcia, J.-P. Adam, J.-V. Kim, J.-F. Roch, I. Miron, G. Gaudin, L. Vila, B. Ocker, D. Ravelosona, and V. Jacques, The nature of domain walls in ultrathin ferromagnets revealed by scanning nanomagnetometry, Nat. Commun. **6**, 6733 (2015).

[8] C. S. Wolfe, V. P. Bhallamudi, H. L. Wang, C. H. Du, S. Manuilov, R. M. Teeling-Smith, A. J. Berger, R. Adur, F. Y. Yang, and P. C. Hammel, Off-resonant manipulation of spins in diamond via precessing magnetization of a proximal ferromagnet, Phys. Rev. B **89**, 180406(R) (2014).

[9] C. Du, T. van der Sar, T. X. Zhou, P. Upadhyaya, F. Casola, H. Zhang, M. C. Onbasli, C. A. Ross, R. L. Walsworth, Y. Tserkovnyak, and A. Yacoby, Control and local measurement of the spin chemical potential in a magnetic insulator, Science **357**, 195 (2017).

[10] P. Andrich, C. F. de las Casas, X. Liu, H. L. Bretscher, J. R. Berman, F. J. Heremans, P. F. Nealey, and D. D. Awschalom, Long-range spin wave mediated control of defect qubits in nanodiamonds, NPJ Quantum Inf. **3**, 28 (2017).

[11] E. Lee-Wong, R. Xue, F. Ye, A. Kreisel, T. Van Der Sar, A. Yacoby, and C. R. Du, Nanoscale detection of magnon excitations with variable wavevectors through a quantum spin sensor, Nano Lett. **20**, 3284 (2020).

[12] J. Trimble, B. Gould, F. J. Heremans, S. S.-L. Zhang, D. D. Awschalom, and J. Berezovsky, Relaxation of a single defect spin by the low-frequency gyrotropic mode of a magnetic vortex, J. Appl. Phys. **130**, 083903 (2021).

[13] M. R. Page, B. A. McCullian, C. M. Purser, J. G. Schulze, T. M. Nakatani, C. S. Wolfe, J. R. Childress, M. E. McConney, B. M. Howe, P. C. Hammel, and V. P. Bhallamudi, Optically detected ferromagnetic resonance in diverse ferromagnets via nitrogen vacancy centers in diamond, J. Appl. Phys. **126**, 124902 (2019).

[14] T. van der Sar, F. Casola, R. Walsworth, and A. Yacoby, Nanometre-scale probing of spin waves using single-electron spins, Nat. Commun. **6**, 7886 (2015).

[15] C. M. Purser, V. P. Bhallamudi, F. Guo, M. R. Page, Q. Guo, G. D. Fuchs, and P. C. Hammel, Spinwave detection by nitrogen-vacancy centers in diamond as a function of probe-sample separation, Appl. Phys. Lett. **116**, 202401 (2020).

[16] D. Rohner, J. Happacher, P. Reiser, M. A. Tschudin, A. Tallaire, J. Achard, B. J. Shields, and P. Maletinsky, (111)-oriented, single crystal diamond tips for nanoscale scanning probe imaging of out-of-plane magnetic fields, Appl. Phys. Lett. **115**, 192401 (2019).

[17] G. Yu, A. Jenkins, X. Ma, S. A. Razavi, C. He, G. Yin, Q. Shao, Q. lin He, H. Wu, W. Li, W. Jiang, X. Han, X. Li, A. C. B. Jayich, P. K. Amiri, and K. L. Wang, Room-temperature skyrmions in an antiferromagnet-based heterostructure, Nano Lett. **18**, 980 (2018).

[18] T. X. Zhou, J. J. Carmiggelt, L. M. Gächter, I. Esterlis, D. Sels, R. J. Stöhr, C. Du, D. Fernandez, J. F. Rodriguez-Nieva, F. Büttner, E. Demler, and A. Yacoby, A magnon scattering platform, PNAS **118**, e2019473118 (2021).

[19] I. Lee, Y. Obukhov, G. Xiang, A. Hauser, F. Yang, P. Banerjee, D. V. Pelekhov, and P. C. Hammel, Nanoscale scanning probe ferromagnetic resonance imaging using localized modes, Nature **466**, 845 (2010).

[20] Y. Obukhov, D. V. Pelekhov, J. Kim, P. Banerjee, I. Martin, E. Nazaretski, R. Movshovich, S. An, T. J.

Gramila, S. Batra, and P. C. Hammel, Local Ferromagnetic Resonance Imaging with Magnetic Resonance Force Microscopy, Phys. Rev. Lett. **100**, 197601 (2008).

[21] F. Guo, L. M. Belova, and R. D. McMichael, Spectroscopy and Imaging of Edge Modes in Permalloy Nanodisks, Phys. Rev. Lett. **110**, 017601 (2013).

[22] G. Wu, S. P. White, W. T. Ruane, J. T. Brangham, D. V. Pelekhov, F. Yang, and P. C. Hammel, Local measurement of interfacial interactions using ferromagnetic resonance force microscopy, Phys. Rev. B **101**, 184409 (2020).

[23] A. Volodin, C. Van Haesendonck, E. Skorokhodov, R. Gorev, and V. Mironov, Ferromagnetic resonance force microscopy of individual domain wall, Appl. Phys. Lett. **113**, 122407 (2018).

[24] A. W. Schell, G. Kewes, T. Schröder, J. Wolters, T. Aichele, and O. Benson, A scanning probe-based pick-and-place procedure for assembly of integrated quantum optical hybrid devices, Rev. Sci. Instrum. **82**, 073709 (2011).

[25] S. I. Bogdanov, O. A. Makarova, A. S. Lagutchev, D. Shah, C.-C. Chiang, S. Saha, A. S. Baburin, I. A. Ryzhikov, I. A. Rodionov, A. V. Kildishev, A. Boltasseva, and V. M. Shalaev, Deterministic integration of single nitrogen-vacancy centers into nanopatch antennas, ArXiv:1902.05996v1 (2019).

[26] A. Vansteenkiste, J. Leliaert, M. Dvornik, M. Helsen, F. Garcia-Sanchez, and B. Van Waeyenberge, The design and verification of MuMax3, AIP Adv. **4**, 107133 (2014).

[27] R. D. McMichael and B. B. Maranville, Edge saturation fields and dynamic edge modes in ideal and nonideal magnetic film edges, Phys. Rev. B **74**, 024424 (2006).

[28] V. S. Bhat, S. Watanabe, K. Baumgaertl, A. Kleibert, M. A. W. Schoen, C. A. F. Vaz, and D. Grundler, Magnon Modes of Microstates and Microwave-Induced Avalanche in Kagome Artificial Spin Ice with Topological Defects, Phys. Rev. Lett. **125**, 117208 (2020).

[29] S. Kempinger, Y.-S. Huang, P. Lammert, M. Vogel, A. Hoffmann, V. H. Crespi, P. Schiffer, and N. Samarth, Field-Tunable Interactions and Frustration in Underlayer-Mediated Artificial Spin Ice, Phys. Rev. Lett. **127**, 117203 (2021).